Journal of
Manufacturing and Materials Processing

MDPI

Article

Influence of Printing Parameters on the Morphological Characteristics of Plasma Directed Energy-Deposited Stainless Steel

Luis Segovia-Guerrero [1,*], Antonio José Gil-Mena [2], Nuria Baladés [3], David L. Sales [4], Carlota Fonollá [4], María de la Mata [5] and María de Nicolás-Morillas [4,†]

[1] INNANOMAT Group, Department of Industrial Engineering and Civil Engineering, IMEYMAT, Algeciras School of Engineering and Technology, University of Cádiz, Ramón Puyol Ave., 11202 Algeciras, Spain
[2] Department of Electrical Engineering, Algeciras School of Engineering and Technology, University of Cádiz, Ramón Puyol Ave., 11202 Algeciras, Spain; antonio.gil@uca.es
[3] IEG Group, Department of Industrial Engineering and Civil Engineering, IMEYMAT, Algeciras School of Engineering and Technology, University of Cádiz, Ramón Puyol Ave., 11202 Algeciras, Spain; nuria.balades@uca.es
[4] INNANOMAT Group, Department of Materials Science and Metallurgical Engineering and Inorganic Chemistry, IMEYMAT, Algeciras School of Engineering and Technology, University of Cádiz, Ramón Puyol Ave., 11202 Algeciras, Spain; david.sales@uca.es (D.L.S.); carlota.fonollasimo@alum.uca.es (C.F.); maria.denicolas@gm.uca.es (M.d.N.-M.)
[5] INNANOMAT Group, Department of Materials Science Metallurgical Engineering and Inorganic Chemistry, IMEYMAT, Faculty of Sciences, University of Cádiz, Universidad de Cádiz Ave., 11510 Puerto Real, Spain; maria.delamata@uca.es
* Correspondence: luis.segovia@uca.es
† Current address: Sustainable Powder Technologies Group, IMDEA Institute, Eric Kandel 2, Tecnogetafe, 28906 Getafe, Spain.

Abstract: This study investigated the influence of printing parameters and strategies on the morphological characteristics of austenitic stainless steel beads deposited on carbon steel substrates, using plasma directed energy deposition (DED). The experimental setup varied the welding current, wire feed speed, and torch travel speed, and we analyzed three printing strategies: simple-linear, overlapping, and oscillating. Moreover, advanced 3D scanning and computational analysis were used to assess the key morphological features, including bead width and height. The results showed that the computational model developed by using parabolic assumptions accurately predicted the geometric outcomes of the overlapping beads. The oscillating printing strategy was the one that showed improved morphological uniformity and bead substrate wettability, so these features were used for multi-layer component manufacturing. The use of equivalent wavelength–amplitude values resulted in maximum combinations of bead height and width. Moreover, cost-effective carbon steel substrates were feasibly used in microstructural and elemental analyses, with the latter ones confirming the alignment of the bead composition with the wire-fed material. Overall, this study provides practical insights for optimizing plasma DED processes, thus enhancing the efficiency and quality of metal component manufacturing.

Keywords: additive manufacturing; WAAM; plasma arc; austenitic stainless steel; wettability; process optimization

Citation: Segovia-Guerrero, L.; Gil-Mena, A.J.; Baladés, N.; Sales, D.L.; Fonollá, C.; de la Mata, M.; de Nicolás-Morillas, M. Influence of Printing Parameters on the Morphological Characteristics of Plasma Directed Energy-Deposited Stainless Steel. *J. Manuf. Mater. Process.* **2024**, *8*, 233. https://doi.org/10.3390/jmmp8050233

Academic Editor: Steven Y. Liang

Received: 31 August 2024
Revised: 27 September 2024
Accepted: 10 October 2024
Published: 15 October 2024

1. Introduction

Additive manufacturing (AM), also known as three-dimensional (3D) printing, refers to manufacturing processes that create 3D parts by building up successive layers of material, without the need for predefined tools, fixtures, or molds, as required in subtractive (milling, turning) or consolidation (casting, molding) manufacturing processes [1,2]. The industrial sector was responsible for 37% of global energy consumption (166 EJ in 2022,

according to the International Energy Agency (IEA) [3]), and for 24% of CO_2 emissions [4], so AM is among the most sustainable technologies, as material waste, energy consumption, and greenhouse gas emissions are significantly reduced. From an economic perspective, AM leads to shorter supply times, thus reducing the losses caused by decreased performance due to breakdowns. Currently, centralized mass production is being replaced by decentralized production in smaller volumes, thus making AM competitive in this new market [5,6].

In the expansive field of AM, many technologies have been developed, and each has been adapted to specific applications and material requirements. Central among these is directed energy deposition (DED), a technology particularly adept at repairing and fabricating metal components. DED involves the fusion of a material, i.e., metal powder or wire, with a concentrated energy source, such as a laser, an electron beam, or plasma, to build a structure layer by layer on a substrate. This method, which processes many materials, is known for its versatility [7,8].

A prominent branch within DED is the plasma arc–wire arc additive manufacturing (PA–WAAM) process. This innovative approach combines the principles of PA welding with wire-based feedstock, to make large metal parts [9,10]. The integration of plasma offers advantages over other heat-source technologies, such as higher deposition rates and improved control over thermal input, which is crucial for maintaining material properties [11,12]. These attributes make WAAM, and especially PA–WAAM, an attractive option for industries to create large, complex metal components with minimal material waste and reduced production time [13,14]. Recent advancements in the PA–WAAM technique have focused on enhancing accuracy, reducing errors commonly associated with high-temperature manufacturing processes, and finding new techniques, like multiple wire feed, that PA–WAAM allows, to obtain better as-produced results. Tsurumaki et al. [15] included sophisticated control systems to optimize thermal management and to improve structural integrity. Additionally, advancements in process modeling and control technologies, as discussed by Kopf et al. [16], have been pivotal in pushing the boundaries of what can be achieved by PA–WAAM, particularly in the aerospace and automotive sectors. Moreover, Feng et al. [17] proposed an innovative and high-efficiency process to fabricate Cr-Ni stainless steel components through a double-wire process. The deposition rate was increased 1.06 times, the ultimate tensile strength (UTS) was increased by 10.2%, and elongation was increased by 176% as maximum.

In all AM processes, including PA–WAAM, bead morphology must be controlled, to obtain optimal structural integrity and the mechanical properties of fabricated parts. For this purpose, characteristics such as bead width, height, penetration, overlap, and bead substrate wettability angles should be accurately measured and analyzed. These characteristics are increasingly being measured using advanced capture methods and are being evaluated by sophisticated computational tools.

Various technologies are used to capture the morphological characteristics of a weld bead. These technologies can be divided into two groups. The first group includes techniques that rely on conventional sensors, such as ultrasound, X-ray, spectroscopy, and infrared thermography. The second group is based on 2D and 3D vision systems, where cameras and lasers are commonly used [18]. Matlab (MathWorks Corporation, Natick, MA, USA), with its strong data-processing and visualization capabilities, is used to process the data obtained from 3D scanning technologies and experimental observations, allowing for a detailed quantitative analysis of bead geometry [19,20]. Beyond the scope of traditional computational fluid dynamics (CFD), custom coding simulations are used to simulate thermal and metallurgical dynamics during bead formation. These simulations predict the effects of various printing parameters on bead morphology, providing valuable insights for process optimization. Matlab and coding simulations have been used to develop predictive models that can accurately forecast the outcomes of different welding scenarios. These models, which are validated against experimental results, are useful tools for refining the PA–WAAM process. Furthermore, potential defects are found early, and process parameters

are adjusted to reduce them, thus enhancing both the quality and the consistency of the manufactured parts [21,22].

This study aimed to provide a thorough evaluation of how operating parameters (i.e., intensity, wire feed speed, and travel speed) and printing strategies (i.e., simple-linear, overlapping, and oscillating) impact the morphological and micro-structural characteristics of the initial austenitic stainless steel beads deposited on a carbon steel substrate using PA–WAAM.

2. Materials and Methods

2.1. Materials

An AISI 316LSi stainless steel 1.2 mm diameter wire was deposited on a carbon steel substrate, using PA–WAAM and various combinations of parameters, thus obtaining a set of beads to be studied. Table 1 provides the nominal composition of the wires, as provided by the manufacturer (Nippon Gases Ltd., Navarra, Spain). The substrate was made of an AISI 1040 carbon steel sheet with dimensions of 250 × 160 mm^2 and a thickness of 10 mm. Carbon steel plates are commonly used for substrates, mainly for economic reasons, even when the wire feed material is different.

Table 1. Nominal composition of the AISI 316LSi wire.

Elements (wt.%)						
Cr	**Ni**	**Mo**	**Mn**	**Si**	**C**	**Fe**
18.5	12.0	2.7	1.7	0.9	0.02	balance

2.2. PA–WAAM Bead Deposition

An ADDILAN model P1200-4X-I (Addilan Fabricación Aditiva S.L., Durango, Spain) was used. The equipment is based on Cartesian axes and is equipped with a Tetrix 552 AC/DC Synergic Plasma AW GR (SCO 4103) generator and a T drive 4 Rob 3 RE HW, both parts from EWM (Mündersbach, Germany). Wire feed speeds up to 5.0 m/min can be reached. This machine also features a PMW 350-2 torch that deposits material, using current up to 350 A. All parameters, including voltage, were monitored in real time throughout the printing process, to ensure that the layers were deposited at a consistent torch height. These conditions included current intensity, voltage, wire feed speed (WFS), torch travel speed (TS), plasma gas flow rate (PGFR), and shielding gas flow rate (SGFR). The gas used was argon (Ar), with 99.999% purity (Ar-5.0). Based on previous tests, the settings were adjusted to suit both the PA–WAAM equipment and the material under study. The operating parameters for deposition are presented in Table 2. PGFR and SGFR were set to 1.2 lpm and 12 lpm, respectively.

Table 2. Experimental printing parameters of beads.

Parameter	Units	Simple-Linear	Overlapping	Oscillating
Wire feed speed, WFS	m/min	2, 4.4	2	4.4
Torch travel speed, TS	mm/min	300	300	300
Current, *I*	A	235, 255, 265, 285	265	285
Step-over increment, *p*	mm	-	3.0, 3.5, 4.0, 4.5, 5.0	-
Oscillating amplitude	mm	-	-	5, 6, 7, 8
Oscillating spatial wavelength	mm	-	-	6, 7, 8, 9

This study consisted of three separate experimental setups for the deposition of simple-linear, overlapping, and oscillating beads, and it was conducted on separate substrates. Firstly, eight simple-linear beads (Figure 1a) were produced. The TS was kept constant, and the WFS and electric current systematically varied. Secondly, overlapping beads were made (Figure 1b). Two single beads were overlapped with constant welding parameters, with an

overlap distance ranging from 3 to 5 mm in 0.5 mm steps. Finally, an oscillating bead path (Figure 1c) characterized by a square waveform was employed, a piecewise linear function that was described by alternating horizontal (x-direction) and vertical (y-direction) segments, forming a square wave-like path when plotted. This function was not continuous but consisted of linear segments that created a regular, repeating structure. The pattern was defined by the G-code, which directed the welding torch to alternate its position along the x-axis while moving forward incrementally along the y-axis. In this final set of experiments, the amplitude and the spatial wavelength of the wave path varied, while the WFS, TS, and current were constant and identical to the settings of the second experiment.

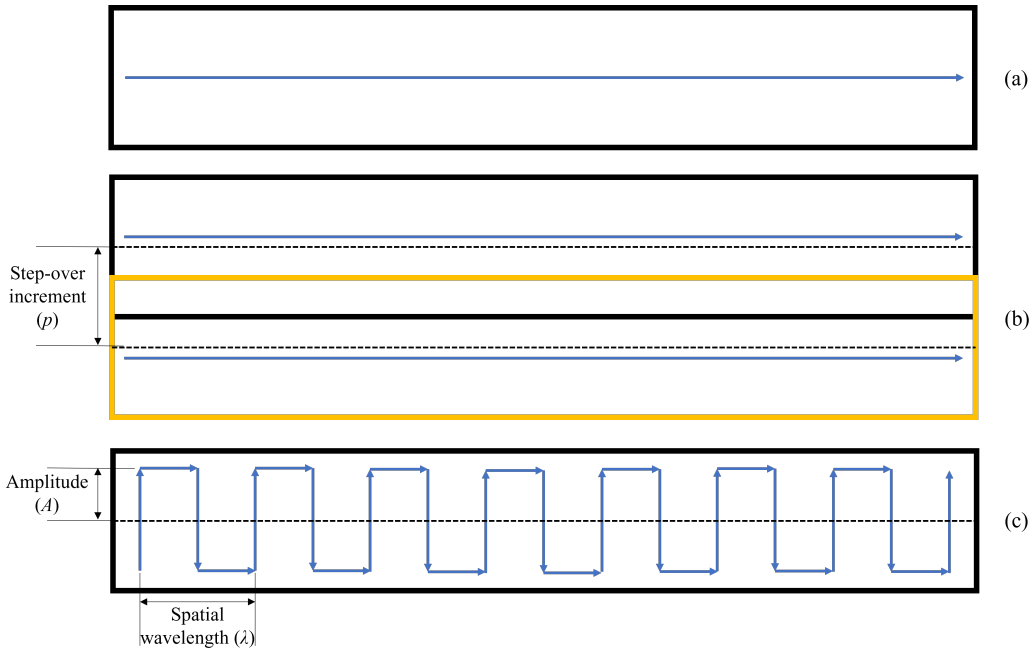

Figure 1. (**a**) Trajectory for a linear bead; (**b**) trajectories for overlapping beads; (**c**) trajectory for oscillating bead.

2.3. Morphological Characterization

A MetraSCAN Black Elite 3D scanner was used for digitizing the printed beads. It is an optical coordinate-measuring machine (CMM) from Creaform (Creaform Inc., Québec, Canada). The device has a high accuracy of 0.025 mm, along with a measurement resolution of the same magnitude and a mesh resolution of 0.100 mm, thus ensuring detailed dimensional data capture of components, regardless of their size, material, finish, or complexity. It features 15 blue laser crosses and one additional line that efficiently captures detailed geometric data, even on reflective surfaces. After collecting the dimensional data, the acquired information was processed using the VXelements software (version 11, Creaform Inc., Levis, QC, Canada. The mesh was inspected, cleaned, aligned, and exported in STL format.

Upon acquiring the STL file, a post-processing methodology was implemented, to isolate the beads and to extract their principal characteristics. While commercial software dedicated to such analyses is available, the authors chose the Matlab programming language for its inherent versatility, modularity, and greater capacity for customization. The employed methodology consisted of five steps:

1. The first step involved centering and rotating the board. This step required the orientation of the triangulated object within the STL file, to align the deposition process direction with the x-axis. This adjustment was manually performed through visual inspection of the projection on the XY plane.
2. The second step focused on trimming each aligned bead, by enclosing it within a rectangular prism (see yellow rectangles in Figure 2c), thus leading to trimming and

delineation. Two distances were set for the beginning and end of the bead (x-axis limits), according to whether the measurements covered the bead's entire length or whether truncation was needed, due to irregular geometry at its start and finish [23].

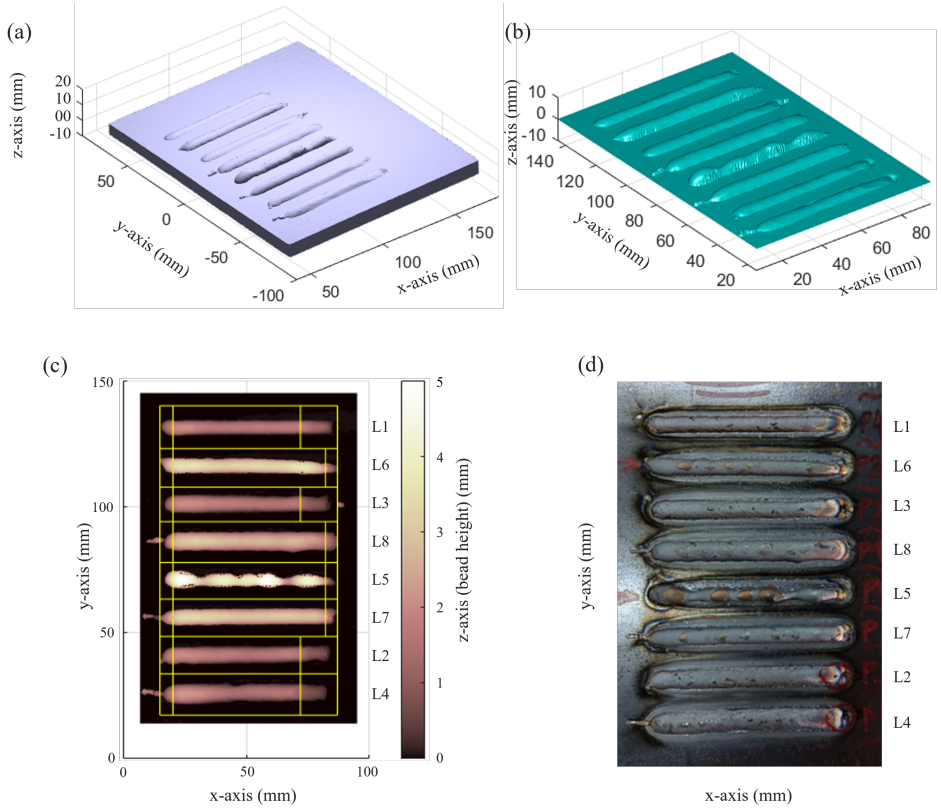

Figure 2. Representations of the morphology and picture of the simple (linear) WAAM printed beads: (**a**) raw scanned model showing a slightly bent surface due to heat input; (**b**) surface after bending correction; (**c**) plan-view of the bending-corrected scanned surface, showing bead height in temperature–color scale, and the trimming sections in yellow boxes; and (**d**) picture of the actual plate.

3. The third step involved correcting the deformation of the substrate after depositing the beads, to identify accurately the sections. This correction was based on evaluating the height of the grid used in bead trimming, with all the points corresponding to the substrate zero plane of the substrate. A mesh generated by linear interpolation was then subtracted from the scanned substrate, thus neutralizing the initial deformation.
4. After converting the triangulated object (composed of points and triangles) into a mesh matrix, using 3D interpolation, the fourth step involved sectioning the bead along its length, to obtain several cross-sections, which corresponded to the increment used on the x-axis of the interpolation.
5. However, not all sections derived from this process, which entailed calculating bead height and width, were considered. Sections with spurious points (i.e., the beads affected by melt spillage or exhibiting keyholes) were discarded. Additionally, some sections at bead commencement and conclusion were also excluded, particularly those where the cross-sectional pattern did not match the typical bead shape. This fifth step consisted of calculating a constant and representative bead height and cross-section. To identify and remove such erroneous sections, three criteria were established by leveraging the least squares method for section identification via parabolas [24,25]:
    - Sections identified as parabolas that did not intersect with the x-axis (with complex roots) were removed.
    - Sections were removed when the discrepancy between the area of the scanned bead section (A_s) and the area of the corresponding identified parabola (A_p)

exceeded the threshold given by Equation (1). This threshold was proportional to the average of all the analyzed section areas:

$$|A_p - A_s| > k(\overline{|A_p - A_s|}) \quad (1)$$

- Sections where the ratio of the negative area (A_s^-) to the positive area (A_s^+) of the scanned section exceeded a set threshold proportional to the average of all the section ratios, as it is described in Equation (2), were also removed:

$$\frac{A_s^-}{A_s^+} > k\overline{\left(\frac{A_s^-}{A_s^+}\right)} \quad (2)$$

The variables in Equations (1) and (2) are defined as follows: A_p is the area beneath the identified parabola and the x-axis; A_s is the area beneath the scanned section and the x-axis; k is the proportional constant (with a value of 5 used in this study); A_s^+ is the positive area under the scanned section and x-axis; and A_s^- stands for the negative area under the x-axis and the scanned section. The width and height of all the sections were ascertained (i.e., the width from the span of the identified parabola, and the height from the maximal elevation of the bead section). Afterward, an average of the dimensions of the sections was computed. The quality of the scanning process and calculations was assessed by comparing the volume of the bead calculated by the scanned sections with the volume derived from the bead average width and height.

2.4. Microstructural Characterization

To prepare the samples for their microstructural study, a Struers Labotom (Struers LLC, Cleveland OH, USA) disc cutter was used to transversely cut the bead substrate assemblies. Afterward, the parts were embedded in a thermoset conductive resin with a Struers Citopress-1. To prepare the surfaces, grinding grits from 240 to 1200 P were used, polishing with 3 mm and 1 mm diamond suspensions and finishing with OPS colloidal silica. The samples were electrochemically etched by immersing them in a 65% nitric acid solution and by applying an electric current of 0.02 A at 6 V for 1 min.

After preparing sample surfaces, a Nikon Epiphot 200 inverted optical microscope (Nikon Corporation, Tokyo, Japan) was used to observe them. SEM–EDS (scanning electron microscope–energy-dispersive X-ray spectroscopy) analysis was performed with Tescan Vega 4 equipment (Tescan, Brno, Czech Republic), to study the phases, structure, and composition of the samples. This SEM microscope was provided with a tungsten electron gun and equipped with a 4-quadrant backscattered electrons (BSEs) retractable detector designed for the acquisition of BSE, in addition to a secondary electrons detector, providing simultaneous topographic and chemical information on the samples, and it was accompanied by chemical composition mapping, thanks to its EDS detector controlled throughout by TESCAN Essence™. The samples for the SEM were etched by aqua regia solution.

2.5. Wettability Angle Measurement

One approach to evaluating the quality of deposited beads on a substrate is by measuring the wettability angles, which is a cost-efficient method, in terms of material consumption. This technique involves capturing the contact angle between the bead and the substrate surface, using an image obtained from a camera adapted to an optical microscope. The contact angle value is influenced by the surface tension of the phases involved, including the liquid (molten metal), solid (substrate), and vapor. This relationship, first described by Young in the 19th century [26], is given by the equation $\gamma_{sv} - \gamma_{sl} = \gamma_{lv} \cos\theta$, where γ_{sv}, γ_{sl}, and γ_{lv} represent the surface tensions of the solid–vapor, solid–liquid, and liquid–vapor interfaces, respectively, and θ is the contact angle.

The deposited beads' wettability angles were measured through image analysis, using scientific image-processing software (ImageJ [27]). These measurements were conducted by optical micrographs of the bead substrate cross-section taken with a 5x optical lens. To have

more precision during measurement, due to better contrast, the outer angle between the bead and the substrate was measured. This angle (α) corresponded to the supplementary of the experimental wettability or contact angle (θ), as described in Equation (3):

$$\theta = 180^{\circ} - \alpha \tag{3}$$

3. Results and Discussion

3.1. Simple Beads

Figure 2 shows the first, second, and third steps described in Section 2.3 in relation to the morphological analysis of simple beads before extracting them from the substrate. Figure 2b presents one of the experimental plates after rectifying the bending deformation of the substrate because of heat transfer, and Figure 2c shows the projection onto the XY plane and the delineation of each bead. The x-limits of each bead varied according to whether the assessment encompassed all the bead sections or excluded the initial and terminal segments of the bead.

All cross-sections were overlaid, to study the progression of a bead along its length. This technique was used to obtain qualitative data of the uniformity of bead height and width, and it was used as an indicator of quality. Figure 3 presents bead cross-sections. The sections that met the three criteria outlined in the fifth step of Section 2.3 are drawn.

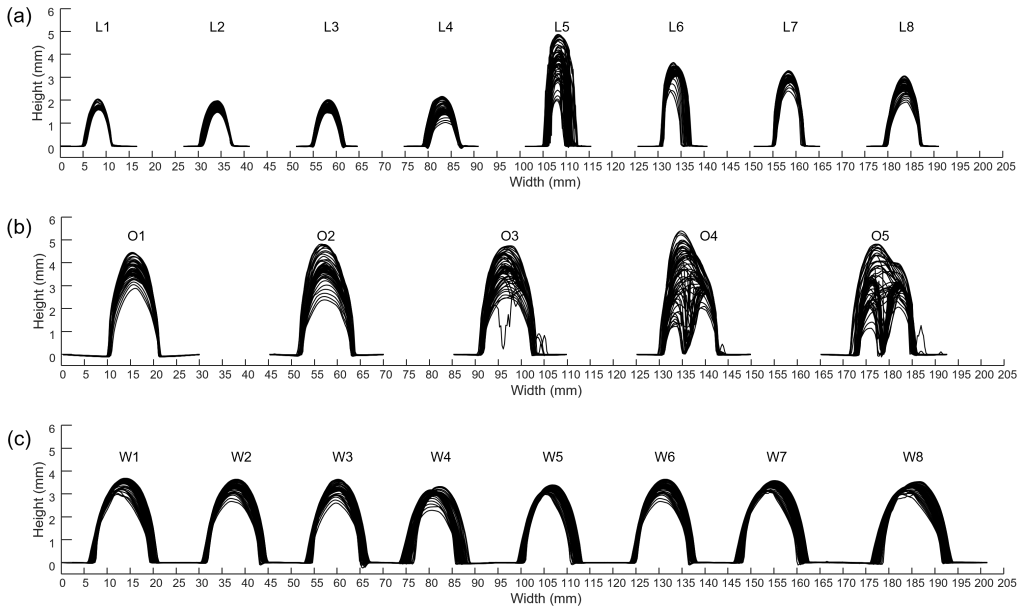

Figure 3. Superimposed cross-sections extracted along the length of the WAAM printed beads for (**a**) simple-linear beads, (**b**) overlapping beads, and (**c**) oscillating beads. The x-axis distance values are intended for relative measurements within a single bead.

Table 3 includes the data obtained from the scanned linear beads (graphically shown in Figure 3a), although omitting the initial and final portions, together with the processing parameters. The bead characteristics were measured by sectioning them at intervals of 0.176 mm, which yielded a total of 293 (L1 to L4) and 351 (L5 to L8) sections, according to the bead length. Consequently, the values presented in Columns 4, 5, and 6 represent the average values of the maximum height ($\overline{h}$), the estimated maximum height ($\overline{\widehat{h}}$), and the estimated width ($\overline{\widehat{w}}$) across all sections, respectively. The estimated height and width were calculated from the identified parabolas, using a least squares approach, to minimize the norm. $\widehat{N}$ is the average norm, while $\overline{\sigma_{h_{max}}}$, $\overline{\sigma_{\widehat{h}}}$, and $\overline{\sigma_{\widehat{w}}}$ are the standard deviations of the maximum height, the estimated height, and the estimated width, respectively. L and V

are the length of the bead and the volume of the scanned sections, respectively. $\widehat{V}$ is the volume calculated using the estimated height and width given by Equation (4).

$$\widehat{V} = \frac{2}{3} L \widehat{h} \widehat{w} \tag{4}$$

Table 3. Resultant geometrical parameters of the linear beads. The PA–WAAM parameters are also included. The TS was 300 mm/min in all cases.

Bead ID	WFS (m/min)	I (A)	$\overline{h}$ (mm)	$\overline{\widehat{h}}$ (mm)	$\overline{\widehat{w}}$ (mm)	$\overline{N}$ (mm)	$\overline{\sigma_{h_{max}}}$ (mm)	$\overline{\sigma_{\widehat{h}}}$ (mm)	$\overline{\sigma_{\widehat{w}}}$ (mm)	L (mm)	V (mm^3)	$\widehat{V}$ (mm^3)	θ
L1	2.0	235	1.7906	1.8114	5.9840	0.1257	0.1335	0.1323	0.2254	51.7	373.77	373.60	43°
L2	2.0	255	1.7648	1.7957	6.7890	0.1259	0.1508	0.1617	0.3906	51.7	420.04	420.18	42°
L3	2.0	265	1.7767	1.7972	6.7934	0.1203	0.1802	0.1812	0.5478	51.7	421.77	420.80	41°
L4	2.0	285	1.7402	1.7530	7.4102	0.1419	0.2895	0.2904	0.6582	51.7	442.19	447.74	99°
L5	4.4	235	3.8649	4.0093	5.9618	1.2435	0.7179	0.7550	1.2779	61.9	925.76	986.38	142°
L6	4.4	255	3.3694	3.4618	7.0206	0.6075	0.2250	0.2458	0.6170	61.9	937.78	1002.95	103°
L7	4.4	265	3.0429	3.1061	7.6186	0.4060	0.1836	0.1910	0.2996	61.9	929.13	976.53	100°
L8	4.4	285	2.7111	2.7397	8.4029	0.2726	0.1335	0.1323	0.2613	61.9	924.41	950.03	69°

The deviation was clearly affected by the WFS. At a constant current and TS, there was less deviation when the WFS was lower, so beads L1 to L4 showed less deviation than the others. On the other hand, the deviation decreased as the current increased in the beads printed with higher WFS (the beads from L5 to L8). Consequently, a current of 235 A along with a WFS of 4.4 m/min should not be used.

Figure 4 shows the impact of the current on bead width and height under two distinct WFSs. When the current increased, the width of the bead also increased, especially at higher wire feed speeds. On the other hand, increasing the current reduced the height of the bead. This impact was more significant at higher wire speeds, while there was no difference at lower speeds (2 m/min). It is crucial to stress that these observations were made while the TS was constant at 300 mm/min. Therefore, all beads except L5 were considered valid, regarding their morphology. The selection of one over another would depend on the desired width and height outcomes. Additionally, it is also important to note that the choice of operating parameters, particularly in terms of higher or lower energy input, would slightly impact the composition of the beads after deposition, as will be discussed in the EDX analysis in Section 3.5.

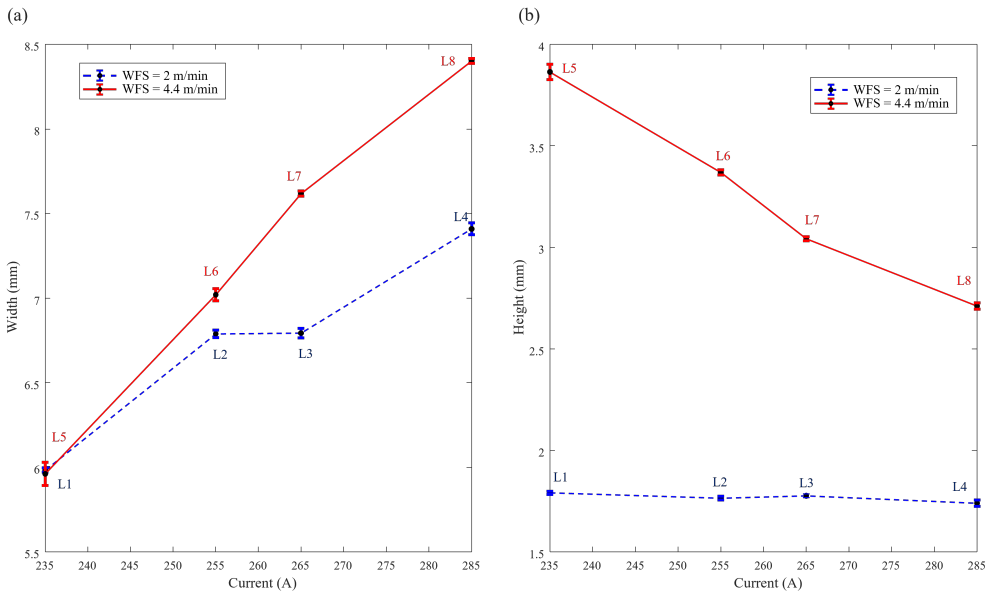

Figure 4. Bead width (**a**) and height (**b**) as a function of the printing current for the two WFSs.

3.2. Overlapping Beads

The cross-sectional bead profiles of the overlapping beads (from O1 to O5) printed with various configurations were analyzed, using a parabola model. This approach provided a good fit for most overlapping beads, except when the bead overlap was not successful. The height and width of the parabola were used to define the models for bead overlap. Five beads were produced, each with two inner beads using different step-over increments, denoted as p. The overlapping distances for these beads were set at 3.0, 3.5, 4.0, 4.5, and 5.0 mm (see Table 2). All the overlapping beads were made under consistent parameters of current intensity, TS, and WFS, which were maintained at 265 A, 300 mm/min, and 2 m/min, respectively.

Figure 3b shows the overlapping sections of the five beads. Beads O1 and O2 seamlessly overlapped without any gaps. On the other hand, beads O4 and O5 did not overlap properly in many sections. Bead O3 seemed to be borderline, in terms of proper overlap. According to these observations, the critical overlap limit (or critical center distance for stable multi-bead overlapping processes, as defined by Ding et al. [28]), was around 3.5 mm, which corresponded to 4.9 mm between the axes of the beads (the step-over increment). This critical overlap limit was dependent on the wire-fed diameter.

The data included in Table 4 outline the characteristics of the scanned beads, such as the distance between their axes (p), as well as the parameters previously included in Section 3.1 and Table 3. Beads O4 and O5 showed a greater error (least mean square norm) when compared to the original beads. That error was consistent with the visual information shown in Figure 3b.

Table 4. Resultant geometrical parameters of the overlapping beads.

Bead ID	p (mm)	$\overline{h}$ (mm)	$\overline{\hat{h}}$ (mm)	$\overline{\hat{w}}$ (mm)	$\overline{N}$ (mm)	$\overline{\sigma_{h_{max}}}$ (mm)	$\overline{\sigma_{\hat{h}}}$ (mm)	$\overline{\sigma_{\hat{w}}}$ (mm)	L (mm)	V (mm^3)	$\hat{V}$ (mm^3)	θ
O1	3.0	3.779	3.844	12.318	0.587	0.387	0.409	0.379	72	2186.596	2272.69	133°
O2	3.5	3.839	3.889	12.774	0.691	0.530	0.531	0.625	88	2806.141	2914.42	87°
O3	4.0	3.835	3.845	13.521	1.059	0.588	0.619	1.128	88	2828.875	3049.63	43°
O4	4.5	3.790	3.574	19.526	2.150	0.873	1.065	12.885	88	2824.109	4094.50	83°
O5	5.0	3.522	3.260	25.070	2.602	0.672	0.904	36.045	88	2785.406	4793.97	103°

Figure 5a includes a model that shows the relationship among the various geometric parameters, to predict the outcome of overlapping beads, using parabolas [25,28]. This model was based on two assumptions:

- Both the original and the resulting beads were modeled as parabolas.
- The width of the resulting bead was equal to the width of the original bead plus the step-over increment, which was the distance between the axes of the two initial beads.

Consequently, when the step-over increment (p), the height (h), and the width (w) of the original beads were known, the dimensions of the resulting bead (both h and w) could be deduced, as shown in Figure 5a. Under the assumption that the area of the resulting bead was the sum of the areas of the original beads (Equation (5)), and in conjunction with Equation (6), the height of the resultant bead could be calculated, using Equation (7):

$$A_o = A_1 + A_2 = 2\left(\frac{2}{3}hw\right) = \frac{2}{3}h_o w_o \tag{5}$$

$$w_o = w + p \tag{6}$$

$$h_o = 2hw/(w + p) \tag{7}$$

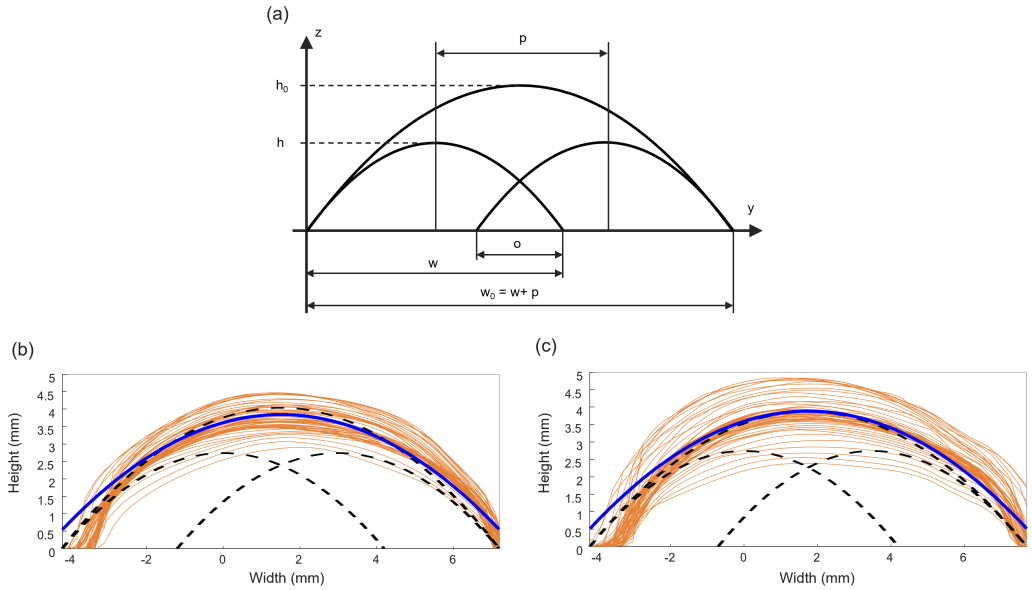

Figure 5. Model bead profile for two overlapping beads (**a**). Theoretical (dashed lines) versus actual bead profiles, resulting in overlapped beads O1 (**b**) and O2 (**c**). The blue lines are the estimated profile, and the orange lines are the different cross-sections of the overlapped beads.

A_1 and A_2 are the theoretical sections corresponding to the overlapping linear beads; A_0 is the resulting section after the overlap. Similarly, h and w represent the original height and width, respectively, of the single linear beads and h_0, w_0 the height and width result after the overlap. The simple-linear bead chosen by using the specified deposition parameters was, therefore, bead L3 (see Table 3). Figure 5b,c show the actual bead cross-sections in comparison with the theoretical parabolas derived from beads O1 and O2. Figure 5a is the schematic diagram that illustrates the theoretical model of the overlapping beads, where w is the width of one bead, p is the distance between the peaks of the two overlapping beads (i.e., the overlapping length), o is the overlap distance, w_o is the total distance of the resulting overlap, h is the height of each bead, and h_o is the height of the resulting overlap. Figure 5b,c are plots that compare the theoretical model (which is shown in solid blue and black dashed lines) with actual data (which are shown by multiple thin orange lines that represent the different cross-sections along the overlapped beads). In these figures, the x-axis represents the width and the y-axis represents the height. The blue solid line indicates the theoretical height profile of the overlapping beads; that profile is a parabola, which was estimated using the least squares method for all the experimental sections. This line should be compared to the theoretical one, which is the black dashed line corresponding to the profile after the overlap. The black dashed lines represent the theoretical single beads that overlap, thus producing the single overlapped bead. The orange lines represent the multiple data sets obtained from the cross-section of the overlapping bead.

As for the fitting of the experimental results to the model, the blue solid line follows the general trend of the orange lines. The variation in the actual data represented by the orange lines shows some deviation, although with a reasonable fit.

In this case, the optimal overlap distance for the wire diameter used and the deposition conditions employed was approximately 3.5 mm. The overlap limit (step-over distance, p) was around 4.0 mm, beyond which more irregular sections or double beads (i.e., areas where there was no overlap) began to appear.

3.3. Oscillating Beads

In this experiment, the beads were printed according to an oscillatory linear or zig-zag pattern, varying the amplitude and wavelength (see Figure 1c). The current, WFS, and TS

were constant at 285 A, 300 mm/min, and 4.4 m/min, respectively, for all seven experiments (Table 2). Figure 3c shows the superimposed cross-sections of the beads. The method involved keeping one parameter constant while changing the other. Consequently, beads W2 and W6 were duplicates of the same experiment. The results of the morphological analysis for the oscillating beads are presented in Table 5.

Table 5. Resultant geometrical parameters of the oscillating beads, and the values of the two processing parameters under study: wavelength (wl.) and amplitude (ampl.).

Bead ID	wl. (mm)	ampl. (mm)	$\overline{h}$ (mm)	$\overline{\widehat{h}}$ (mm)	$\overline{\widehat{w}}$ (mm)	$\overline{N}$ (mm)	$\overline{\sigma_{h_{max}}}$ (mm)	$\overline{\sigma_{\widehat{h}}}$ (mm)	$\overline{\sigma_{\widehat{w}}}$ (mm)	L (mm)	V (mm^3)	$\widehat{V}$ (mm^3)	θ
W1	6	6	3.475	3.539	14.645	0.604	0.166	0.198	0.454	50.0	1679.2	1727.4	69°
W2	7	6	3.312	3.379	14.128	0.551	0.194	0.212	0.501	58.0	1799.4	1845.8	63°
W3	8	6	3.255	3.302	13.217	0.469	0.194	0.215	0.481	67.0	1908.5	1949.3	53°
W4	9	6	3.015	3.070	13.035	0.411	0.194	0.205	0.283	73.7	1931.3	1966.4	86°
W5	7	5	3.166	3.226	13.104	0.441	0.093	0.120	0.394	54.4	1499.9	1533.1	70°
W6	7	6	3.312	3.379	14.128	0.551	0.194	0.212	0.501	58.0	1799.4	1845.8	63°
W7	7	7	3.332	3.388	15.470	0.478	0.116	0.146	0.305	54.4	1862.3	1900.8	69°
W8	7	8	3.300	3.353	16.935	0.470	0.120	0.148	0.204	54.4	2017.5	2059.3	70°

A comparison of Figure 3c with the one depicting the simple beads in Figure 3a reveals a notable difference: the sections were more homogeneous. Thus, the oscillating movement of the torch stabilized the geometry of the bead. This fact, together with the advantage that oscillatory bead deposition allows larger deposited volumes to be obtained in a shorter time, makes this a strategy of special benefit, which deserves further research [29]. The selection of the desired operating parameters for the oscillatory beads will depend on the target width and height. Figure 6 can be used for this selection.

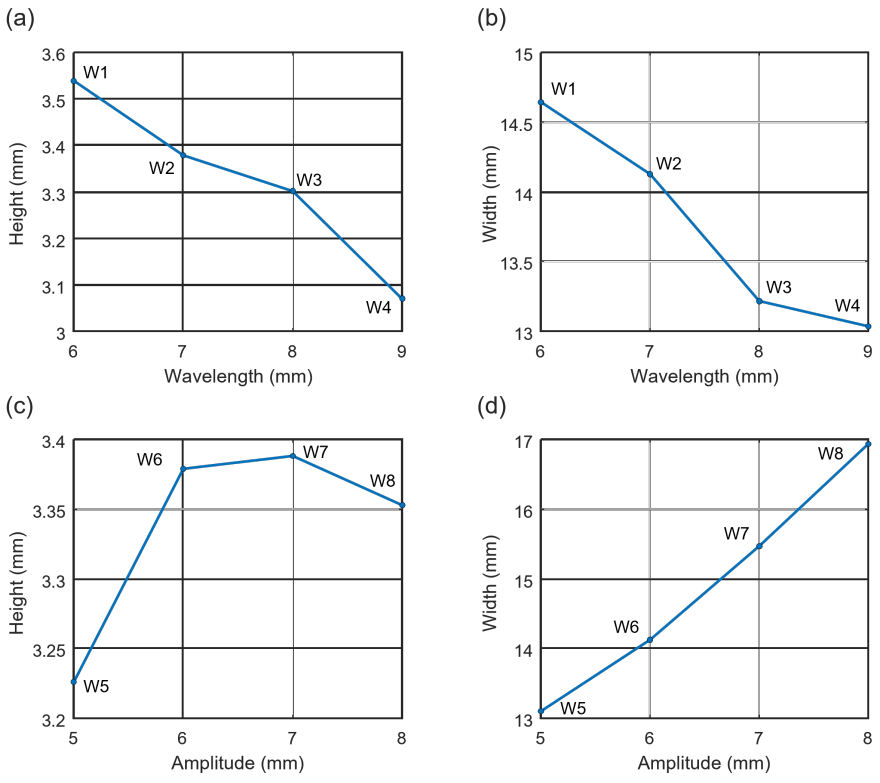

Figure 6. Height and width versus oscillating parameters: wavelength and amplitude. (**a**) Height vs. wavelenght; (**b**) width vs. wavelength; (**c**) height vs. amplitude; (**d**) width vs. amplitude.

3.4. Wettability Analysis

Wettability angles are key indicators in welding processes. In the WAAM process, this parameter shows the spreadability of a liquid (i.e., a molten metal) on a solid surface, which is a metallic substrate. A lower wettability angle suggests that the molten metal wets the surface better, which can result in both a stronger bond and improved material interaction. This angle is affected by surface roughness, processing temperature, and the chemical composition of the materials.

Figure 7 shows some measurements whose wettability angles (θ) were gathered in the last column of Tables 3–5, respectively, for each set of experiments. Figure 7a exhibits a representative sample of all the conducted measurements, comprising a cut cross-section and embedded into bakelite for its microscopy analysis. Figure 7b corresponds to a magnification of Figure 7a, indicated by the yellow square, measured by optical microscopy.

For linear beads, as the current increased there was a general trend toward lower wettability angles, thus indicating improved wetting characteristics at higher energy inputs for a constant WFS, as indicated by Ayarkwa et al. [30] and Jérome [31]. Increasing the WFS from 2.0 m/min to 4.4 m/min implied, in general, higher wettability angles, which could indicate less favorable wetting conditions. The reason could have been a faster cooling rate or changes in the bead geometry at higher deposition rates. These two trends were not present in sample L4.

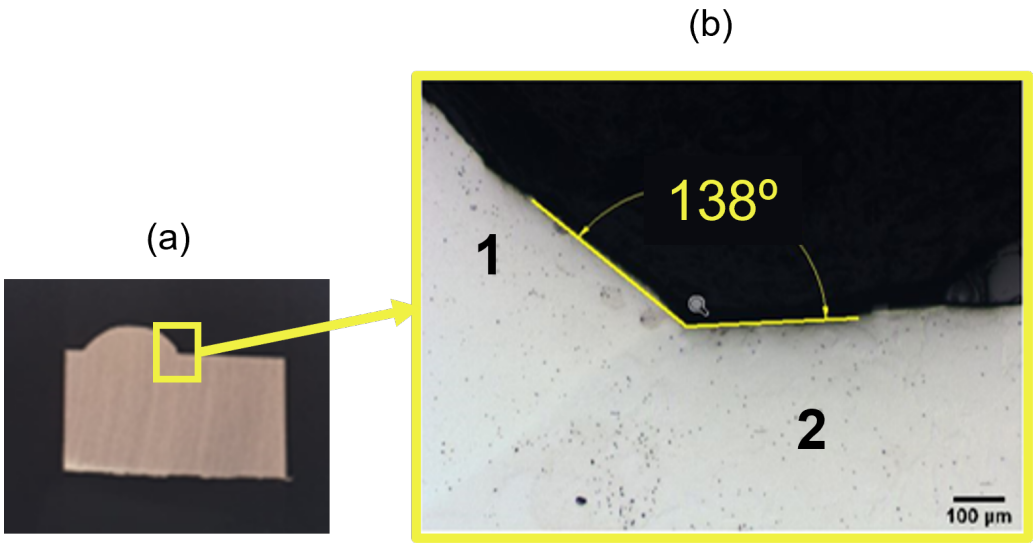

Figure 7. Measured wettability angles (α) of the deposited simple-linear beads at 2 m/min of WFS and a current of 255 A: (**a**) cross-section of the bead, and (**b**) zoom-in of the studied area, where 1 is the deposited bead and 2 is the substrate.

The wettability angles were different in the most successful overlapped beads, as mentioned in Section 3.2 (beads O1 and O3). These beads showed lower angles, which indicated better wetting. Moreover, the wetting quality potentially decreased in beads O4 and O5, whose wettability angles were greater, perhaps due to insufficient heat input or to the increased complexity of the overlapping beads affecting the uniformity of the material spread. It is worth stressing that the best general morphological characteristics (good overlap at low variability along the bead, and low wettability angle) were expected to be reached with a p value between 3.5 and 4.0.

The oscillating beads presented, in general, low wettability angles, thus resulting in more uniform and favorable wetting conditions. The regularity in the wettability angles for the oscillating beads could be attributed to the controlled variation in the amplitude and the wavelength, which enhanced the distribution of the material and the heat during the printing process, as depicted in Wang et al. [32].

3.5. Microstructural Analysis of the Bead–Substrate Interface

Optical microscopy (OM) was performed along the cross-sections of the samples, following the procedure (i.e., sample preparation, etching, and imaging) described in Section 2.4.

Figure 8 shows the optical micrographs of two simple bead samples, representative of the whole set, i.e., L3 (left) and L5 (right). They were selected due to the difference exhibited in their wettability angles and depositing energy, L3 having a higher depositing energy and L5 the lowest of all the set. Figure 8a shows a stitched image taken at 5× magnification of the entire studied sample. Figure 8b shows three different parts of the studied sample at 40× magnification, and Figure 8c represents the same three parts at 100× magnification. The labels 1, 2, and 3 correspond to the 316LSi part of the deposited bead, the bead–substrate interface, and the carbon steel substrate, respectively.

In the regions labeled '1' in Figure 8, the main phase was austenite (γ), as this stainless steel is designed to remain fully austenitic, due to its high nickel content. This phase was face-centered cubic (FCC) and provided the material with its characteristic toughness, ductility, and corrosion resistance. An equiaxed grain structure was visible in both L3 and L5 in these regions. Additionally, as is common in welding or additive processes like the one used, a certain amount of delta ferrite (δ phase) was visible (black dendrites). Delta ferrite is a body-centered cubic (BCC) phase, which is stable at high temperatures and forms during solidification in the liquid state. It tends to transform into austenite as the material cools, but under rapid cooling or non-equilibrium conditions, small amounts of delta ferrite can be retained, typically along grain boundaries, as evidenced by Rizvi and Tewari [33] and by Pereira et al. [34]. The darker inclusions observed in both L3 and L5 were likely M23C6 carbides (where M stands for metals, such as chromium, molybdenum, and iron). These carbides form along grain boundaries during cooling and solidification, particularly in an austenitic matrix. They were thermodynamically stable at the temperatures experienced during the deposition process, and their presence was more likely to be concentrated at the grain boundaries in both samples [35].

In the regions labeled '2', at the bead–substrate interface, the 316L side primarily consisted of austenite, but some delta ferrite was also found, due to the thermal conditions near the interface. The high cooling rates and non-equilibrium solidification could lead to the retention of delta ferrite in this region. On the carbon steel side, the interface was primarily composed of ferrite (α phase), a BCC phase typical of low-carbon steel, and cementite (Fe_3C), particularly within the ferrite–pearlite regions. The cementite phase formed due to the carbon content in the steel, and it tended to be concentrated along the lamellar structure in the pearlite regions (pearlite is a mixture of ferrite and cementite in a lamellar structure). It was a hard and brittle phase. If carbon diffused into the interface from the substrate, there could be localized areas with increased cementite content. The interface in L5 appeared wavy and irregular, potentially indicating more non-uniform solidification and cementite accumulation at the boundary. Some bainite may have been present at the interface on the carbon steel substrate, as studied by Zhai et al. [36].

In the areas labeled '3' within the carbon steel substrate, the primary phases were ferrite and pearlite. The coarser grain structure observed in L5 suggests slower cooling and longer times for grain growth, resulting in more distinct pearlite layers. L3 exhibited a finer grain structure, with smaller lamellar spacing in the pearlite, indicating faster cooling rates and less time for grain growth in the substrate [37].

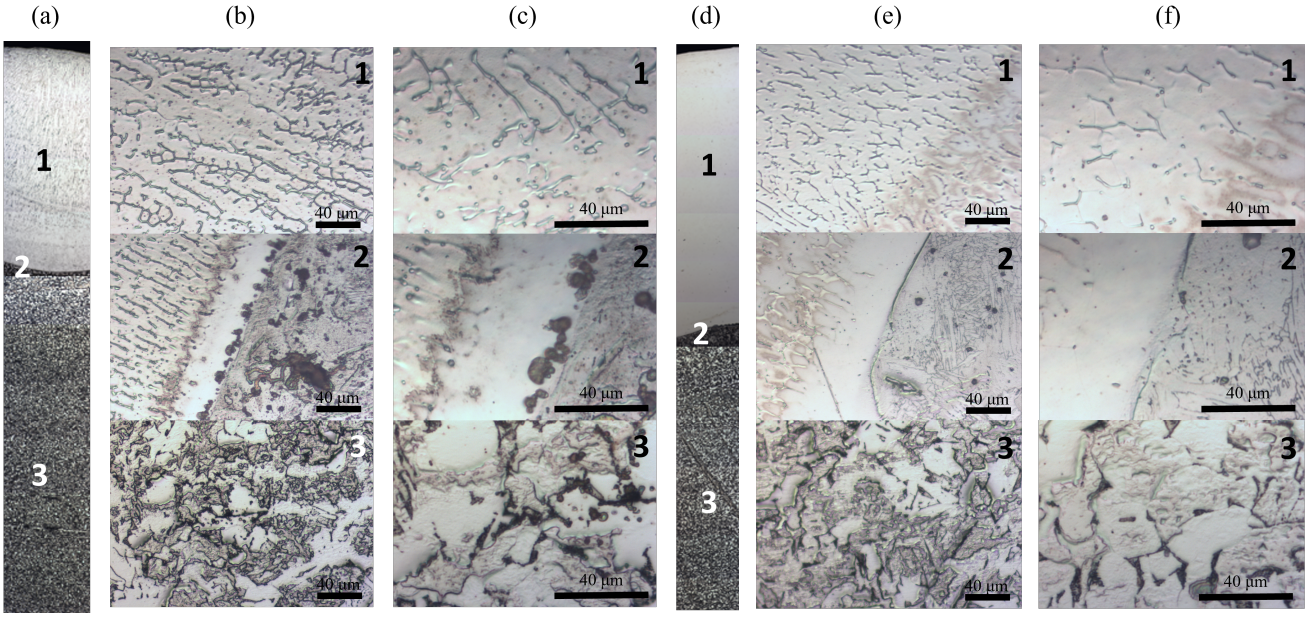

Figure 8. OM analysis of beads L3 (**a**–**c**) and L5 (**d**–**f**): (**a**,**d**) stitching of the bead–substrate assembly, where three areas can be appreciated (1—stainless-steel AISI316L deposited bead, 2—bead–substrate interface, and 3—carbon steel substrate); (**b**,**e**) zoom of each region acquired with a 40× optical lens; and (**c**,**f**) zoom of the regions acquired with a 100× optical lens.

Figure 9 displays the SEM-BSE images of the same samples, providing higher magnification and compositional contrast, which offers information complementary to the OM. Figure 9a corresponds to L3, and Figure 9b corresponds to L5. In these images, three regions were again distinguished: 316L stainless steel bead (green box), bead–surface interface (orange box), and carbon steel substrate (highlighted in purple). The micrographs were acquired at the points indicated by crosses in the photographs on the left, using the same color code. In L3, the SEM images highlighted a uniform, equiaxed grain structure in the 316L stainless steel bead, confirming the observations made in the OM images. The presence of carbide precipitates, particularly M23C6 carbides, was more evident at the grain boundaries in the SEM images. The bead–substrate interface in L3 was smooth and well defined, with clear compositional contrast between the bead and the substrate, indicating minimal mixing during deposition, as the EDX would confirm. This supported the OM findings of a homogeneous defect-free interface. The carbon steel substrate in L3 also exhibited a sharp boundary, with a ferrite–pearlite structure clearly visible. In L5, the images revealed a coarser grain structure in the stainless steel bead compared to L3, with more evident carbide precipitation, likely due to the higher WFS leading to increased turbulence and less uniform solidification. The bead–substrate interface in L5 was more irregular, with a wavy appearance and increased cementite content, as highlighted by the compositional contrast in the SEM images. This wavy pattern was consistent with the OM observations and indicated less controlled solidification at the interface. The carbon steel substrate in L5 showed a coarser microstructure than in L3, with less distinct ferrite–pearlite boundaries, likely due to the combined effects of higher deposition rates and slower cooling. Overall, the correlation between the OM and SEM-BSE analyses underscored that L3 featured a more stable deposition process, with finer grains and a smoother interface, while L5 demonstrated the effects of higher deposition rates, leading to coarser grains and a more irregular interface [36].

To summarize, after the study of all the samples (20 in total), it can be seen that all had an interface between the bead and the substrate with no defects, such as pores or cracks, that could adversely affect the mechanical properties of the deposited material. Moreover, all had similar microstructures. From top of each bead to its bottom, the observations were as follows:

- The beads contained an equiaxed austenite structure with darker inclusions, likely due to the presence of the $M_{23}C_6$ phase that was thermodynamically stable.
- A thin interface showed a sharp transition between stainless steel and carbon steel.
- The substrate exhibited a mix of fine ferrite–pearlite/bainite structure typical of carbon steel, with coarser grains compared to the fine-grained structure of the austenitic stainless steel bead. This difference was expected, due to the variations in cooling rates and the solidification behavior between the two materials.

Figure 10 shows EDX line scans of beads L4, L5, W8, (a), (b), and (c), respectively, with the content of the main alloying elements (i.e., Fe, Cr, and Ni). The profiles were taken from the bottom, the AISI1040 carbon steel substrate, throughout the interface to the AISI 316LSi bead. Furthermore, there were sharp transitions among materials ranging from 50 µm to 100 µm. The highest energy bead (L4) had less transition length than the lowest (L5), being W8 length in the middle of both. The line profiles indicated a sharp decrease in Fe content and a corresponding increase in Cr and Ni levels around the 500 µm position, where the transition between carbon steel and stainless steel occurred. For L4, the transition was sharp, indicating a well-defined interface with minimal interdiffusion, due to the higher heat input. This resulted in a distinct composition. In contrast, L5 exhibited a more gradual transition, suggesting a broader diffusion zone at the interface. The lower current combined with the higher WFS likely caused faster deposition and more melt pool turbulence, leading to increased intermixing between the bead and the substrate. This more gradual transition may have contributed to the wavy interface observed in L5's micrographs. W8, which shared the same current as L4 but with a higher WFS, showed a transition profile that fell between L4 and L5, with a moderately defined interface. The sharper transition compared to L5, but not as sharp as L4, suggests that the combination of higher current and faster WFS in W8 led to a balance between distinct compositional boundaries and some intermixing at the interface.

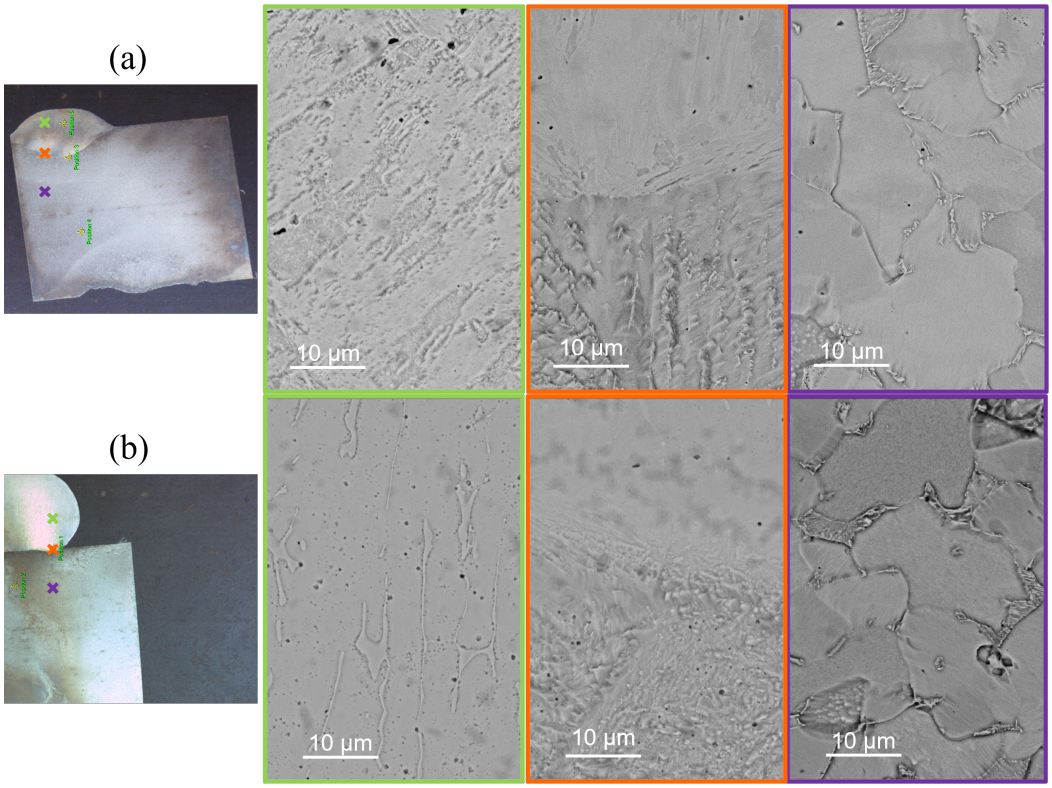

Figure 9. SEM images of bead–substrate assemblies in L3 (**a**) and L5 (**b**) simple-linear beads. In each subfigure, the green colour represents the measurement point on the weld bead, the orange colour represents the point on the interface, and the purple colour represents the point on the substrate, as indicated by the colored crosses in the bead-substrate assembly on the left.

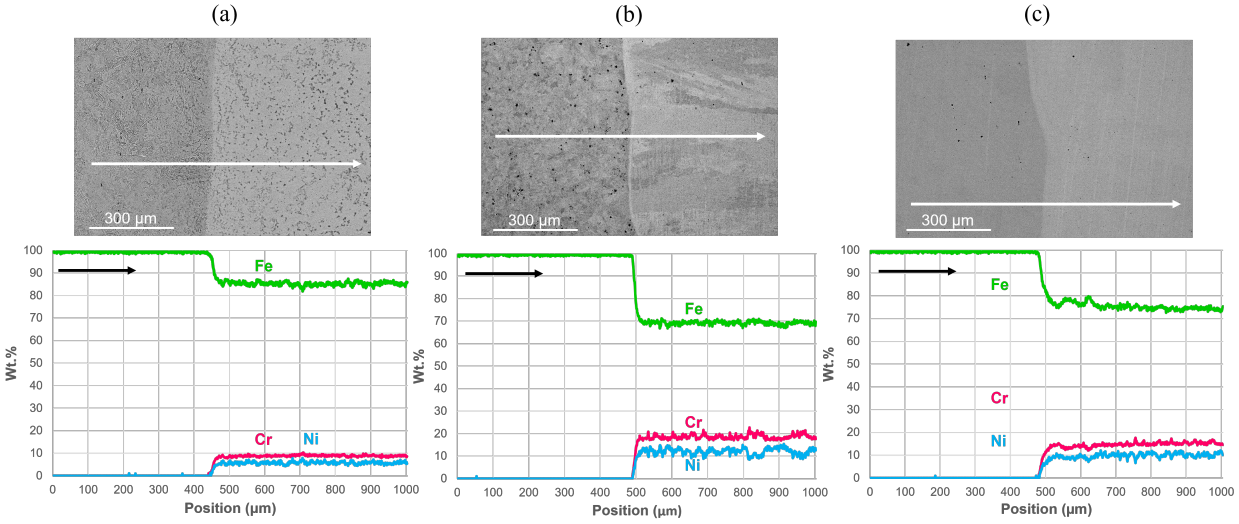

Figure 10. Secondary electrons SEM micrograph of samples L4 (**a**), L5 (**b**), and W8 (**c**). Line profile with the sacnning path is indicated by an arrow in the SEM image (**top row**). Compositional graphs of scanned line in the secondary electrons micrograph (**bottom row**).

Additionally, a point EDX measurement was performed in the middle of the bead in W8, resulting in the chemical composition given by Table 6. This measured composition was like the nominal one given by the wire manufacturer. There were minor variations attributed to both the processing conditions and the limitation for EDX to compute the C content, as it was a light element present in low quantity and under the limit of this examination technique. This analysis ensured that the deposited stainless steel, in a region somewhat away from the interface, maintained its intended chemical properties, which is essential for its application in demanding environments. This outcome shows that cheaper alloys can be used as substrates, thus leading to a more cost-effective manufacturing procedure.

Table 6. EDS-measured composition at a point in the center of the bead in W8.

Elements (wt.%)					
Cr	**Ni**	**Mo**	**Mn**	**Si**	**Fe**
15	10	1	2	1	balance

4. Conclusions

This study has examined the impact of various printing parameters on the morphological and microstructural characteristics of AISI 316LSi stainless steel deposited beads, using the PA–WAAM additive manufacturing technique on carbon steel substrates. Three bead-deposition strategies, i.e., linear, overlapping, and oscillating, were studied, so this work provides critical insights into optimizing the PA–WAAM process for enhanced performance and efficiency.

Combining advanced 3D scanning techniques with computational modeling is a robust framework for accurately assessing the quality and geometry of deposited beads. Our key findings reveal that WFS and current intensity in simple-linear beads significantly influence their morphology. Specifically, lower WFS results in more stable and consistent bead depositions, while higher current intensity can offset the adverse effects of the increased WFS, thus reducing deviations in bead geometry. As for overlapping bead strategies, bead overlap quality is closely tied to the step-over increment (p), with a critical limit of 3.5 mm identified for optimal overlap because of the materials used and the wire diameter (1.2 mm). In addition, the parabolic model successfully predicts the geometrical outcomes of overlapping beads.

The oscillating bead strategy produces more uniform cross-sections and obtains lower and more consistent bead–substrate wettability angles, regardless of the printing parame-

ters. Nevertheless, the use of equivalent wavelength–amplitude values implies maximum combinations in the height–width of the deposited beads. As a result, this deposition strategy has the potential to manufacture industrial components, as larger volumes of material can be printed more efficiently.

The microstructural analysis showed a defect-free interface between the deposited stainless steel and carbon steel substrates in all the samples. It is worth stressing that there was a high WFS that introduced microwaves at the bead–substrate interface, perhaps because of the increased turbulence in the melt pool. Finally, the EDS analysis verified the chemical consistency of the stainless steel bead after deposition, i.e., cost-efficient carbon steel can be used as a substrate because it does not affect the final product.

Author Contributions: Conceptualization, L.S.-G., M.d.N.-M. and D.L.S.; methodology, L.S.-G., M.d.N.-M. and A.J.G.-M.; software, L.S.-G., M.d.N.-M., A.J.G.-M., C.F. and M.d.l.M.; validation, L.S.-G., A.J.G.-M. and N.B.; formal analysis, C.F., N.B. and D.L.S.; resources, D.L.S.; writing—original draft preparation, L.S.-G., M.d.N.-M., A.J.G.-M., M.d.l.M. and D.L.S.; writing—review and editing, L.S.-G., D.L.S., N.B. and M.d.N.-M.; visualization, A.J.G.-M. and M.d.l.M.; supervision, N.B., D.L.S. and M.d.N.-M.; project administration, D.L.S.; funding acquisition, D.L.S. All authors have read and agreed to the published version of the manuscript.

Funding: This research was funded by the Spanish Ministerio de Ciencia e Innovación (project reference EQC2019-006374-P), Junta de Andalucía (research group INNANOMAT ref. TEP-946), the University of Cadiz's Support and Stimulus Plan for Research and Transfer 2022–2023 and the II Call for research project grants of the Cepsa Foundation Chair 2023, project: Industrial maintenance with additive manufacturing: a sustainable paradigm for the circular economy and energy transition. Reference: CCep2023-3. Co-funding from UE is also acknowledged. L. Segovia-Guerrero acknowledges the grant 'Proyecto Singular UCA-SEA-3' from UCA. Finally, M. de Nicolás-Morillas acknowledges the economic support of the Spanish Government (Agencia Estatal de Investigación) and the European Union through the 'Margarita Salas' grant.

Data Availability Statement: The raw data supporting the conclusions of this article will be made available by the authors on request.

Acknowledgments: The authors would like to thank Francisco Gallego for his help on electrochemical etching and OM image acquisition.

Conflicts of Interest: The authors declare no conflicts of interest.

Abbreviations

The following abbreviations are used in this manuscript:

3D	three-dimensional
AISI	American Iron and Steel Institute
AM	additive manufacturing
BSE	backscattered electrons
CFD	computational fluid dynamics
CMM	coordinate-measuring machine
DED	directed energy deposition
EDS	energy-dispersive X-ray spectroscopy
IEA	International Energy Agency
OM	optical microscopy
OPS	oxide polishing suspension
PA	plasma arc
PGFR	plasma gas flow rate
SEM	scanning electron microscopy
SGFR	shielding gas flow rate
TS	torch travel speed
WAAM	wire arc additive manufacturing
WFS	wire feed speed

References

1. Berman, B. 3-D printing: The new industrial revolution. *Bus. Horizons* **2012**, *55*, 155–162. [CrossRef]
2. Attaran, M. The rise of 3-D printing: The advantages of additive manufacturing over traditional manufacturing. *Bus. Horizons* **2017**, *60*, 677–688. [CrossRef]
3. IAE. Industrial Energy Consumption by Fuel in the Net Zero Scenario, 2000–2030—Charts, Data & Statistics. 2022. Available online: https://www.iea.org/data-and-statistics/charts/industrial-energy-consumption-by-fuel-in-the-net-zero-scenario-2000-2030 (accessed on 3 June 2024).
4. IAE. Global Energy-Related CO_2 Emissions by Sector—Charts, Data & Statistics. 2020. Available online: https://www.iea.org/data-and-statistics/charts/global-energy-related-co2-emissions-by-sector (accessed on 3 June 2024).
5. Ben-Ner, A.; Siemsen, E. Decentralization and Localization of Production: The Organizational and Economic Consequences of Additive Manufacturing (3D Printing). *Calif. Manag. Rev.* **2017**, *59*, 5–23. [CrossRef]
6. Koller, J.; Häfner, R.; Döpper, F. Decentralized Spare Parts Production for the Aftermarket using Additive Manufacturing—A Literature Review. *Procedia CIRP* **2022**, *107*, 894–901. [CrossRef]
7. Dass, A.; Moridi, A. State of the Art in Directed Energy Deposition: From Additive Manufacturing to Materials Design. *Coatings* **2019**, *9*, 418. [CrossRef]
8. Mukherjee, T.; Elmer, J.W.; Wei, H.L.; Lienert, T.J.; Zhang, W.; Kou, S.; DebRoy, T. Control of grain structure, phases, and defects in additive manufacturing of high-performance metallic components. *Prog. Mater. Sci.* **2023**, *138*, 101153. [CrossRef]
9. Reisgen, U.; Sharma, R.; Oster, L. Plasma multiwire technology with alternating wire feed for tailor-made material properties in wire and arc additive manufacturing. *Metals* **2019**, *9*, 745. [CrossRef]
10. Wang, C.; Suder, W.; Ding, J.; Williams, S. The effect of wire size on high deposition rate wire and plasma arc additive manufacture of Ti-6Al-4V. *J. Mater. Process. Technol.* **2021**, *288*, 116842. [CrossRef]
11. Duan, X.; Li, Q.; Xie, W.; Yang, X. Wire arc metal additive manufacturing using pulsed arc plasma (PAP-WAAM) for effective heat management. *J. Mater. Process. Technol.* **2023**, *311*, 117806. [CrossRef]
12. Qi, Z.; Cong, B.; Qi, B.; Sun, H.; Zhao, G.; Ding, J. Microstructure and mechanical properties of double-wire+arc additively manufactured Al-Cu-Mg alloys. *J. Mater. Process. Technol.* **2018**, *255*, 347–353. [CrossRef]
13. Li, J.L.Z.; Alkahari, M.R.; Rosli, N.A.B.; Hasan, R.; Sudin, M.N.; Ramli, F.R. Review of wire arc additive manufacturing for 3D metal printing. *Int. J. Autom. Technol.* **2019**, *13*, 346–353. [CrossRef]
14. Klobčar, D.; Baloš, S.; Bašić, M.; Djurić, A.; Lindič, M.; Ščetinec, A. WAAM and Other Unconventional Metal Additive Manufacturing Technologies. *Adv. Technol. Mater.* **2020**, *45*, 1–9. [CrossRef]
15. Tsurumaki, T.; Tsukamoto, S.; Chibahara, H.; Sasahara, H. Precise additive fabrication of wall structure on thin plate end with interlayer temperature monitoring. *J. Adv. Mech. Des. Syst. Manuf.* **2019**, *13*, JAMDSM0028. [CrossRef]
16. Kopf, T.; Glück, T.; Gruber, D.; Staderini, V.; Eugui, P.; Fritze, G.; Mansouri, A.; Schnall, M.; Meyer-Heye, P. Process modeling and control for additive manufacturing of Ti-6Al-4V using plasma arc welding - methodology and experimental validation. *J. Manuf. Process.* **2024**, *126*, 12–23. [CrossRef]
17. Feng, Y.; Zhan, B.; He, J.; Wang, K. The double-wire feed and plasma arc additive manufacturing process for deposition in Cr-Ni stainless steel. *J. Mater. Process. Technol.* **2018**, *259*, 206–215. [CrossRef]
18. Pinto-Lopera, J.E.; Motta, J.M.S.; Alfaro, S.C.A. Real-time measurement of width and height of weld beads in GMAW processes. *Sensors* **2016**, *16*, 1500. [CrossRef] [PubMed]
19. Dinovitzer, M.; Chen, X.; Laliberte, J.; Huang, X.; Frei, H. Effect of wire and arc additive manufacturing (WAAM) process parameters on bead geometry and microstructure. *Addit. Manuf.* **2019**, *26*, 138–146. [CrossRef]
20. Veiga, F.; Suarez, A.; Aldalur, E.; Artaza, T. Wire arc additive manufacturing of invar parts: Bead geometry and melt pool monitoring. *Meas. J. Int. Meas. Confed.* **2022**, *189*, 110452. [CrossRef]
21. Lee, J.; Prabhu, V. Simulation modeling for optimal control of additive manufacturing processes. *Addit. Manuf.* **2016**, *12*, 197–203. [CrossRef]
22. Kumar, P.; Jain, N.K.; Sawant, M.S. Modeling of dimensions and investigations on geometrical deviations of metallic components manufactured by μ-plasma transferred arc additive manufacturing process. *Int. J. Adv. Manuf. Technol.* **2020**, *107*, 3155–3168. [CrossRef]
23. Wang, Z.; Zimmer-Chevret, S.; Léonard, F.; Abba, G. Improvement strategy for the geometric accuracy of bead's beginning and end parts in wire-arc additive manufacturing (WAAM). *Int. J. Adv. Manuf. Technol.* **2022**, *118*, 2139–2151. [CrossRef]
24. Vora, J.; Pandey, R.; Dodiya, P.; Patel, V.; Khanna, S.; Vaghasia, V.; Chaudhari, R. Fabrication of Multi-Walled Structure through Parametric Study of Bead Geometries of GMAW-Based WAAM Process of SS309L. *Materials* **2023**, *16*, 5147. [CrossRef]
25. Suryakumar, S.; Karunakaran, K.P.; Bernard, A.; Chandrasekhar, U.; Raghavender, N.; Sharma, D. Weld bead modeling and process optimization in Hybrid Layered Manufacturing. *CAD Comput. Aided Des.* **2011**, *43*, 331–344. [CrossRef]
26. Young, T. III. An Essay on the Cohesion of Fluids. *Philos. Trans. R. Soc. Lond.* **1805**, *95*, 65–87. [CrossRef]
27. Schneider, C.A.; Rasband, W.S.; Eliceiri, K.W. NIH Image to ImageJ: 25 years of image analysis. *Nat. Methods* **2012**, *7*, 671–675. [CrossRef] [PubMed]
28. Ding, D.; Pan, Z.; Cuiuri, D.; Li, H. A multi-bead overlapping model for robotic wire and arc additive manufacturing (WAAM). *Robot. Comput.-Integr. Manuf.* **2015**, *31*, 101–110. [CrossRef]

29. Ferreira, R.P.; Scotti, A. The concept of a novel path planning strategy for wire + arc additive manufacturing of bulky parts: Pixel. *Metals* **2021**, *11*, 498. [CrossRef]
30. Ayarkwa, K.; Williams, S.; Ding, J. Investigation of pulse advance cold metal transfer on aluminium wire arc additive manufacturing. *Int. J. Rapid Manuf.* **2015**, *5*, 44–57. [CrossRef]
31. Pailhes, J.; Fischer, X.; Villeneuve, F. Phenomenological Model of Thermal Effects on Weld Beads Geometry Produced by Wire and Arc Additive Manufacturing (WAAM). Doctoral Dissertation, Université Grenoble Alpes, Grenoble, France, 2022.
32. Wang, Z.; Zimmer-Chevret, S.; Léonard, F.; Abba, G.; Zeya, W.; Chevret Sandra, Z.; François, L.; Gabriel, A. Prediction of bead geometry with consideration of interlayer temperature effect for CMT based wire-arc additive manufacturing. *Weld. World* **2021**, *65*, 2255–2266. [CrossRef]
33. Rizvi, S.A.; Tewari, S.P. Effect of different welding parameters on the mechanical and microstructural properties of stainless steel 304H welded joints. *Int. J. Eng. Trans. A Basics* **2017**, *30*, 1592–1598. [CrossRef]
34. Pereira, J.C.; Aguilar, D.; Tellería, I.; Gómez, R.; Sebastian, M.S. Semi-Continuous Functionally Graded Material Austenitic to Super Duplex Stainless Steel Obtained by Laser-Based Directed Energy Deposition. *J. Manuf. Mater. Process.* **2023**, *7*, 150. [CrossRef]
35. Rani, K.U.; Kumar, R.; Mahapatra, M.M.; Mulik, R.S.; Świerczyńska, A.; Fydrych, D.; Pandey, C. Wire Arc Additive Manufactured Mild Steel and Austenitic Stainless Steel Components: Microstructure, Mechanical Properties and Residual Stresses. *Materials* **2022**, *15*, 7094. [CrossRef] [PubMed]
36. Zhai, W.; Aishwarya; Shandro, R.; Zhou, W. Microstructure and mechanical properties of the wire arc additively manufactured 316L/ER70S-6 bimetal structure. *Virtual Phys. Prototyp.* **2024**, *19*, e2375105. [CrossRef]
37. Frederic, G.; Voort, V. *Metallography and Microstructures of Stainless Steels and Maraging Steels*; ASM International: Almere, The Netherland, 2004.